FULL PAPER

Thermoacoustic Emission from Carbon Nanotubes Imaged by Atomic Force Microscopy

Daniele Passeri, Ugo Sassi, Andrea Bettucci, Emanuela Tamburri, Francesco Toschi, Silvia Orlanducci, Maria Letizia Terranova, and Marco Rossi*

The thermoacoustic effect of isolated single-wall carbon nanotubes aligned between electrodes is experimentally observed for the first time by imaging the emitted acoustic wave using an atomic force microscopy-based technique specifically developed for the task. The capability of such a technique for single-point thermoacoustic measurements is first verified on carbon nanotubes layers with two electrodes for injecting alternate electric current. The technique is then demonstrated to allow the acquisition, simultaneously with the topography, of images reflecting the pressure of the acoustic wave at fixed distance from the sample. Such a capability is used to collect images reflecting the amplitude of acoustic waves generated by isolated nanotubes and nanotube bundles by the thermoacoustic effect.

1. Introduction

The acoustic emission from conductive wires or thin foils periodically heated by an electric current flowing through them when driven by an alterante voltage, generally referred to as the thermoacoustic effect, was first observed in the second half of the XIXth century.[1] Such an effect was physically understood and modeled and the models were experimentally verified by thermoacoustic loudspeaker (namely, thermophone) prototypes during the first half of the XXth century.[2–4] Briefly, the flow of an alternate electric current with angular frequency ω through a conductive element produces periodical heating due to the Joule effect. This results in the emission, in the medium surrounding the thermoacoustic device, of a temperature wave at angular frequency 2ω, whose amplitude rapidly decays as the distance from the emitter increases. Within this region, the air volume is periodically expanded at angular frequency 2ω as a result of its temperature rising, thus emitting an acoustic wave in the surrounding medium. Conversely, beyond this region the thermal wave can be considered completely attenuated and only the acoustic wave propagates in the medium.

The thermoacoustic effect can be an alternative strategy either to standard piezoelectric transducers or to micromachine diaphragms for the realization of integrated devices for sound reproduction, as the latter do not require any mechanical vibration of the system. In particular, ultrasonic emission in air has been demonstrated from a nanocrystalline Si-based device.[5,6]

In recent years, nanostructured thermoacoustic devices have been proposed, which are based either on an Al nanowire array suspended on a Si substrate,[7,8] or on carbon-nanotube (CNT) assemblies[9–11] In particular, CNT-based devices have been proved to allow the realization of flexible, stretchable and transparent loudspeakers,[9] also suitable for underwater sound generation.[12] All these works investigate the performance of the entire realized devices at the macroscale. Nevertheless, in order to optimize and control the performance of the nanostructured devices, the acoustic emission of the single nastructure should be studied and understood. The performance of a device depends, among other parameters, on the electric conductivity of the single nanostructure, and on its heat capacity and ability to conduct to its surface the heat produced in its interior.[3,9] Therefore, characterization at the nanoscale would allow one to study and verify new nanostructures as the basis of new thermoacoustic devices. Referring to CNT-based devices, the characterization and imaging of thermoacoustic emissions from single nanotubes or single nanotube bundles could allow investigation of the performances of new classes of optimized nanomaterials, for instance CNTs coated by nanodiamond.[13–15] To such purpose, atomic force microscopy (AFM) is the most promising technique, as it allow one to image a sample at the nanoscale by probing it with a tip placed in the close vicinity, which can be used to reveal the CNTs' thermoacoustic emissions. Temperature imaging in electrically heated CNTs has been demonstrated by scanning thermal microscopy,[16,17] which is an AFM-based technique that takes advantage of a specifically realized temperature-sensing tip. Nevertheless, the acoustic

Dr. D. Passeri, Dr. U. Sassi, Dr. A. Bettucci, Prof. M. Rossi
Department of Basic and Applied Sciences for Engineering
University of Rome Sapienza
Via A. Scarpa 16, 00161 Rome, Italy
E-mail: daniele.passeri@uniroma1.it
Dr. E. Tamburri, Dr. F. Toschi, Dr. S. Orlanducci, Prof. M. L. Terranova
Department of Chemical Sciences and Technologies
University of Rome Tor Vergata and Micro and Nano-structured Systems Laboratory (MINASlab)
Via della Ricerca Scientifica, 00133 Rome, Italy
Prof. M. Rossi
Centro di Ricerca per le Nanotecnologie Applicate all'Ingegneria (CNIS), Piazzale A. Moro 5, 00185 Rome, Italy

DOI: 10.1002/adfm.201200435

emission from a single CNT or a single CNT bundle has never been reported.

We report here, for the first time, the direct observation of the thermoacoustic emission from isolated CNTs using a two-pass AFM-based technique that we developed specifically for the purpose; this can obviously be extended to the study of other nanostructures. The technique relies on the detection of the cantilever oscillations produced by an acoustic wave. This idea is completely different from those at the basis of AFM- and scanning near-field optical microscopy (SNOM)-based thermal microscopies, which detect the thermoelastic deformation of the sample or take advantage of thermo-optical or thermoelectric probes.[18,19] The capability of our technique of probing the thermoacoustically emitted sound wave has been first demonstrated by single-point measurements on a single-wall carbon nanotube (SWCNT) layer on glass substrate. Then, its capability of imaging the thermoacoustic emission, collecting maps of the acoustic wavefront amplitude with nanometrical lateral resolution simultaneously to the topographic reconstruction, has been used to detect the acoustic wave generated by isolated SWCNTs aligned between the interdigitated electrode stripes of a multifinger element.

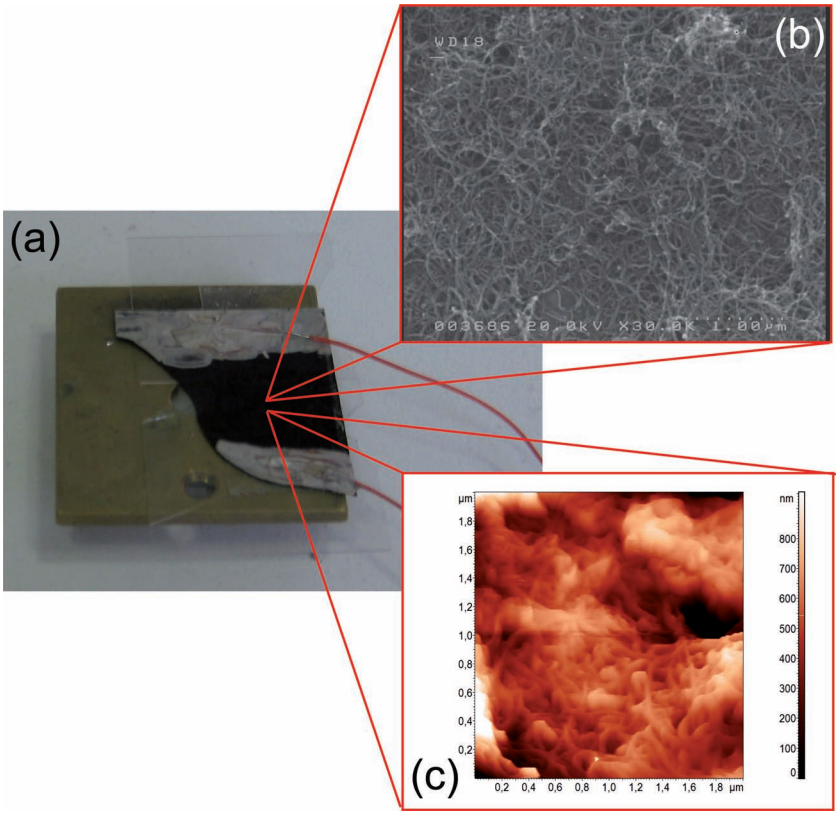

Figure 1. a) Picture of an SWCNT layer sample. Typical SEM (b), and AFM (c) magnifications showing the disordered assembly of SWCNTs forming the film.

2. Experimental Section

2.1. Sample Description

The single-point measurement capability of our technique was demonstrated using SWCNT-layer samples that were obtained by dispersing purified SWCNTs (Cheap Tubes Inc., purity > 90 wt-%, diameter 0.8–1.6 nm, length 5–30 µm) in sodium dodecyl sulfate aqueous solution (1 wt-%). The surfactant was used to achieve a stable and homogeneous dispersion of SWCNTs in water. The starting concentration was 2 wt-% nanotube material. After mixing, the suspensions were sonicated for 4 h. Transparent, conductive layers of nanotubes were fabricated by spray-coating the suspension onto approximately 1.5 × 1.5 cm^2 glass substrates using a conventional airbrush. To avoid droplet formation the substrates were heated to around 100 °C during the deposition. After removing the residual surfactant by rinsing in water, two electrodes were realized on the nanotube network layers by using an Ag conductive glue. **Figure 1**a shows a typical picture of the samples. Two typical magnifications of the SWCNT layer obtained by field-emission scanning electron microscopy (FE-SEM; FE-SEM S-4000, Hitachi) and tapping mode AFM (Dimension Icon, Bruker Inc.) are presented in Figure 1b and c, respectively.

Nanoscale thermoacoustic imaging of electrically heated SWCNTs was performed on samples obtained by depositing the SWCNTs on a multifinger element having an infinite electrical resistance. Such a resistance drops when the nanotubes are uniformly deposited between the interdigitated electrode stripes of the multifinger. Au/Cr thin films were employed as the microelectrode material. The metals were deposited by means of sputtering techniques on SiO_2 insulating layers grown on a p-doped Si substrate. The interdigitated microelectrodes, 5 µm spaced, were patterned by a lift-off technique. The multifinger total size is about 1 cm^2. The samples were realized following the previously optimized procedures reported by Shi et al.[16] The alignment of the nanotubes between the electrodes is then carried out by means of a dielectrophoretic (DEP) method,[20] by applying an AC field with a 1 MHz frequency and 12 Vpp. SEM images of the sample are shown in **Figure 2**.

2.2. Measurement Technique

The acoustic pressure generated by a conductive thin film heated by alternate current is expressed as[9]

$$p\mathrm{rms} = \frac{\sqrt{D}\rho_0}{2\sqrt{\pi}T_0}\frac{P\mathrm{in}}{r}\frac{\sqrt{f}}{C\mathrm{s}}F(f), \quad (1)$$

where *P*rms is the root-mean-square sound pressure; D, ρ_0, and T_0 are the thermal diffusivity, the density, and the temperature

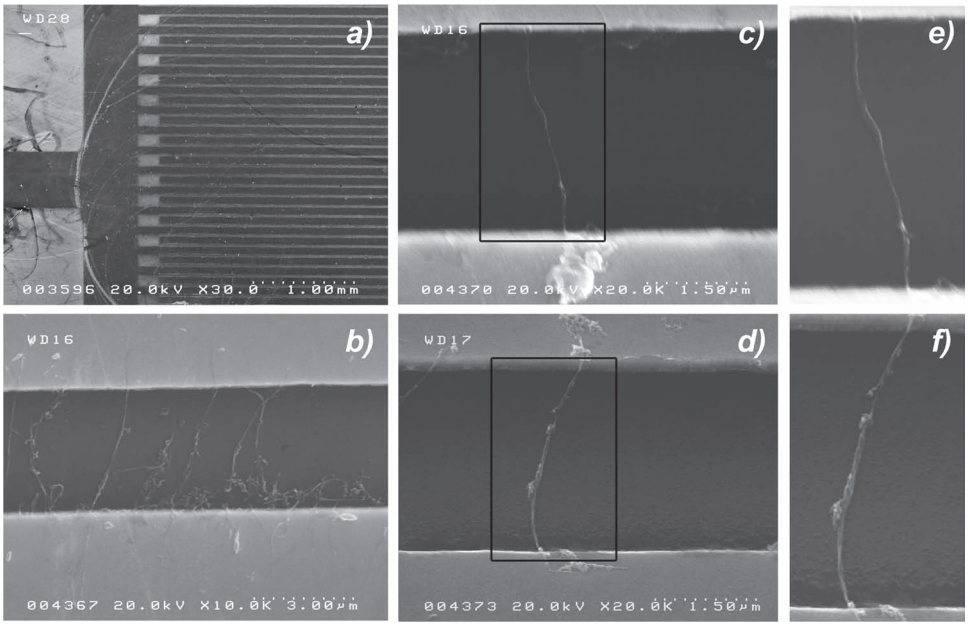

Figure 2. SEM images of different locations of the SWCNT multifinger sample, showing the interdigitated electrodes (a), two opposite electrodes contacted by several SWCNTs (b), isolated SWCNTs contacting two opposite electrodes (c and d), and detail of the SWCNTs (e and f). Agglomerates are visible on both the electrodes edges and the SWCNTs.

of the ambient gas, respectively; P_{in} is the input electric power of the device; r is the distance from the emitting thin film; f is the frequency of sound; C_S is the heat capacity per unit area of the film; and, $F(f)$ is a function of the frequency of sound f, which has been recently derived by Xiao et al.[9] for thin films and layers. For sufficiently thick emitting films, $F(f) \approx 1$,[9] and Equation 1 becomes the one originally deduced by Arnold and Crandall.[3]

For detecting the thermoacoustically emitted sound pressure by AFM, we used the experimental configurations sketched in **Figure 3**a and b for single-point measurements on SWCNT layers and for thermoacoustic imaging of isolated SWCNTs, respectively. Non-essential slight differences in the two experimental configurations from a practical point of view can be recognized in the choice of the cantilever and in its electric connection to the sample, as described in detail in the subsequent section. Conversely, from a general point of view the same technique underlies the two experiments, which is briefly described in the following. The emitting sample is driven at ω by applying to the electrodes an alternate voltage supplied by a signal generator, either an external instrument or that implemented in the AFM itself (i.e., the one used for setting into oscillation the cantilever in standard AFM tapping mode). The thermoacoustically induced pressure wave at 2ω makes the AFM cantilever vibrate at its tip, which is kept at fixed distance Δz from the sample, thus resulting in a modulation of the cantilever deflection signal proportional to the driving force and thus to the acoustic pressure given by Equation 1. The amplitude of the harmonic component at 2ω ($A_2\omega$) in the cantilever deflection signal is detected by a lock-in amplifier, thus allowing single-point thermoacoustic measurements. Moreover, such an idea can be used for thermoacoustic emission imaging by a two-pass AFM technique. In the first pass, the topography of the sample is reconstructed in standard AFM operation modes, i.e., either contact or tapping modes. After each line, the surface profile is used to impose a fixed distance Δz between the tip and the sample. The amplitude $A_2\omega$ is then recorded at each point of the scanned area and its value is used to reconstruct an image reflecting the local value of acoustic pressure at the distance Δz from the emitting surface. As a flexural vibration mode of the cantilever is used, the technique is sensitive to the component of the acoustic wave in the z direction normal to the sample. In principle, the component of the acoustic wave in the x direction (normal to the cantilever length) can be observed using torsional modes of the cantilever. Characterizations of thermoacoustic devices previously reported involved the use of a microphone to detect the emitted signal.[5,7,9,10,12] Conversely, here the acoustic detector is represented by the cantilever, whose mechanical response is highly frequency selective. In principle, the cantilever could detect an acoustic signal at any frequency. Nevertheless, driving the emitting sample at frequency $f_0/2$ (f_0 being the first free flexural resonance frequencies of the cantilever in air) ensures the best possible signal-to-noise ratio. Moreover, sweeping the driving frequency would allow the acquisition of spectra dominated by the mechanical response of the cantilever that should be normalized to the free cantilever spectrum, which would result in an increase of noise and uncertainty due to the cantilever resonance. Finally, to investigate the thermoacoustic effect at different frequencies, either the resonance frequencies of the

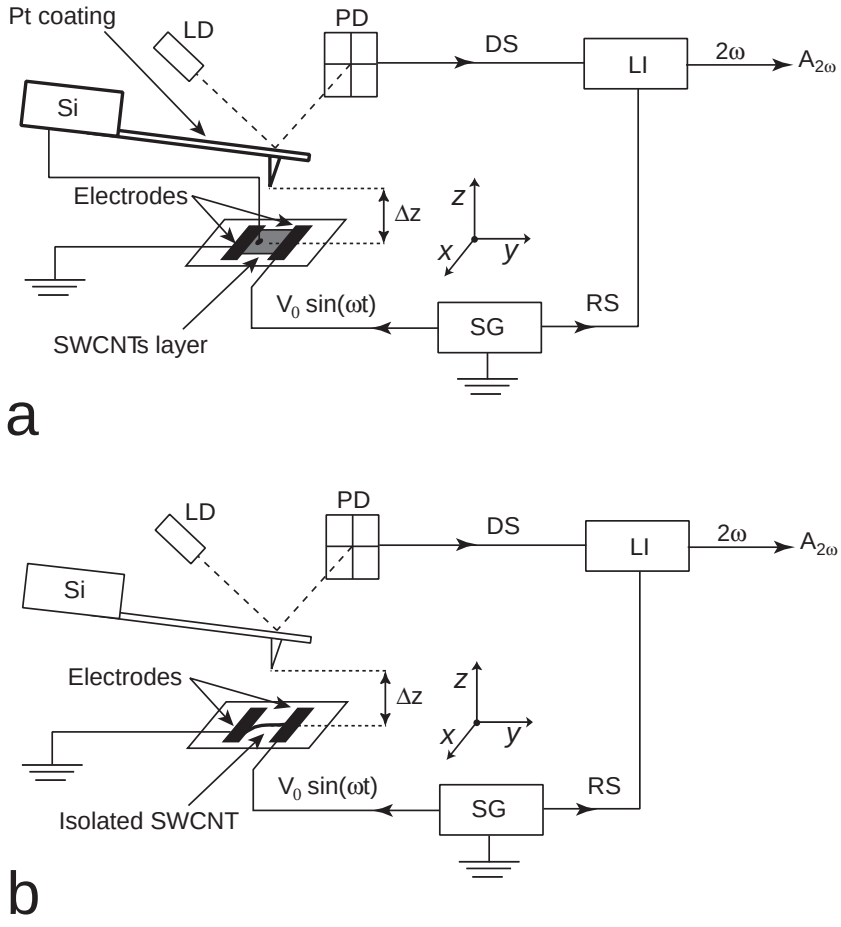

Figure 3. Sketch of the experimental configuration used for AFM thermoacoustic measurements on SWCNTs layers (a) and on isolated SWCNTs aligned between electrodes (b). In both the configurations, the SWCNT sample is excited by an alternate voltage at angular frequency ω supplied by a signal generator (SG). The cantilever deflection is monitored by the beam from a laser diode (LD) reflected by the cantilever back and collected by a photodiode (PD). The vertical deflection signal (DS) is analyzed by a lock-in amplifier (LI) locked to the reference (RS) from the signal generator, thus giving the 2ω signal. For single-point measurements on SWCNT layers, a conductive Pt-coated Si cantilever was used after having realized a short circuit between the cantilever base and the sample in close proximity to the area under the tip (a). For thermoacoustic imaging on isolated SWCNTs, uncoated Si cantilevers were used (b).

higher flexural modes or a set of different cantilevers with different resonance frequencies could be used, in both cases after a proper normalization.

3. Results and Discussion

3.1. Single-Point Measurements: Verification of the Technique

To verify the technique, single-point measurements were performed on the SWCNT-layer samples using the experimental configuration depicted in Figure 3 a. An AFM apparatus (Solver P47H, NT-MDT, Russia) was equipped with a commercial Pt-coated Si cantilever (CSG10/Pt, NT-MDT, Russia) with f_0 = 15.4 kHz. To reduce their electrostatic interaction, an electric short circuit was realized between the tip and the sample by connecting the cantilever base to the SWCNTs layer in close proximity to the sample area under the tip through a thin Pt wire. In the range of frequencies of the cantilever resonance, the impedance of the sample was observed to be purely resistive with a resistance $R_{\text{CNTs layer}}$ = 920 Ω, as measured by a network/spectrum analyzer (4195A, Hewlett-Packard). The amplitude $A_2\omega$ was measured by a lock-in amplifier (SR 530, Stanford Research Systems) external to the AFM apparatus, as a function of either the amplitude V_0 of the alternate driving voltage at frequency $f_0/2$ = 7.7 kHz or the tip sample distance Δz, in order to verify that the cantilever oscillation was caused by the thermoacoustic effect as described by Equation 1. **Figure 4**a shows the measured values of $A_2\omega$ as a function of V_0 (symbols) with the nonlinear fit using the equation $y = ax^2$ superimposed, as suggested by Equation 1. $A_2\omega$ is observed to be proportional to the square of V_0, i.e., proportional to Pin. Analogously, Figure 4b reports the measured value of $A_2\omega$ as a function of Δz (symbols), superimposed by the nonlinear fit using the equation $y = a/(x - b)c$, where $r = x - b$. The parameter b was used to take into account a possible miscalculation of the tip–sample contact point. The parameter c was obtained from the fit and found to be as high as $c = 1.0 \pm 0.1$, thus confirming the proportionality with $1/r$ as predicted by Equation 1. Note that the values of Δz in Figure 4b are higher than the thermal diffusion length $l = \sqrt{D/\pi f}$ [3,12] (approximately 22 μm for $f = f_0$), thus allowing one to neglect the effect of the thermal wave. These results confirm that the cantilever oscillation in our technique is a direct measurement of the acoustic sound pressure produced by thermoacoustic effect.

3.2. Thermoacoustic Imaging of Isolated SWCNTs

To detect the thermoacoustic emission from isolated SWCNTs, the experimental configuration depicted in Figure 3b was used. Here, the realization of an electric short circuit between tip and sample not being possible, standard Si cantilevers were used. Note that standard Si cantilevers are made by slightly doped and thus sightly conductive Si. **Figure 5**a shows images of three SWCNT bundles connecting the two electrodes, obtained in AFM standard tapping-mode using a Si cantilever with f_0 = 171 kHz. At these frequencies, the resistance of the sample is 720 Ω. To obtain the acoustic emission image, in the second pass the excitation of the cantilever was turned off, the sample was driven at frequency $f_0/2$ = 85.5 kHz, and the $A_2\omega$ signal was measured by the internal lock-in

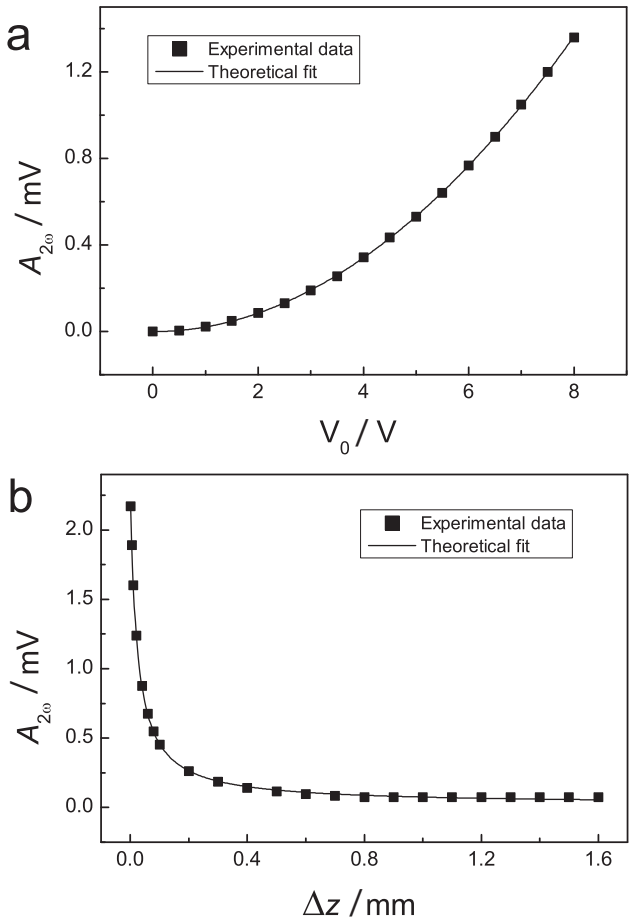

Figure 4. $A_2\omega$ acoustic signal as a function of the alternate voltage amplitude V_0 (a) and of the tip-sample distance Δz (b) measured on an SWCNT-layer sample, with the corresponding fitted curves based on Equation 1.

amplifier of the AFM apparatus (note that the $A_2\omega$ values obtained by the external and the internal lock-in amplifiers are proportional and expressed in millivolts and nanoamperes, respectively). The corresponding $A_2\omega$ image, obtained with Δz = 50 nm is reported in Figure 5 b. The detail of one SWCNT bundle is reported in Figure 5 c. Maps of $A_2\omega$ were then collected for different values of Δz. The images corresponding to Δz = 50, 150, 250, and 350 nm, reported in Figures 5d to g, respectively, clearly show the thermoacoustic emission from the SWCNTs and the electrodes. In particular, the $A_2\omega$ signal corresponding to the SWCNTs shows an appreciable decrease as a function of the distance, while a more moderate one is observed corresponding to the electrodes. The background signal, which can be evaluated from the free area between the electrodes on the right of the SWCNT in Figures 5d to g, is almost independent of the distance, decreasing from 10 nA (near the electrodes) to 8 nA (in the center of the free area). Note that, although the cantilever is set into oscillation at its resonance frequency, the $A_2\omega$ detected signal is extremely low. Performing cantilever oscillation amplitude measurements as a function of the tip–sample distance, 1 nA in the acoustic images of Figure 5 is estimated to correspond to 0.4 nm and therefore, the maximum value of $A_2\omega$ corresponds to about 6 nm. For comparison, at the same frequency the cantilever set-point amplitude was 65 nm for acquisition of the topographical images in Figure 5.

Figure 6 a shows a topographic image of an SWCNT bundle between the electrodes, acquired using a Si cantilever with f_0 = 175.5 kHz. Figure 6b shows the profile of $A_2\omega$ for different values of Δz, acquired in correspondence with the dashed line in Figure 6 a. As Δz increases, the amplitude of the $A_2\omega$ curve as well as its quality factor decreases, as expected for a propagating cylindrical wave. At these frequencies the thermal diffusion length can be evaluated as l = 6 μm, which is higher than the Δz values used. Therefore, the tip is not probing the region of purely acoustic wave propagation and consequently the $A_2\omega$ images results from the contribution of both the acoustic and the thermal waves. Nevertheless, the effect of the thermal wave can be regarded as a periodical dilatation of the cantilever resulting in additive noise in the 2ω signal. Note also that: i) the detected acoustic emission signal results from the contribution of only the air region between the tip and the sample, rather than the entire air volume affected by the temperature oscillation; ii) the emitting sample has a 1D (i.e., is a nanotube) instead of a 2D (i.e., a homogeneous layer) geometry; and, iii) with increasing distance between the aligned SWCNT and the AFM tip, the latter also starts to detect the thermoacoustic wave generated by the metal electrodes. These considerations prevent one from analyzing the decrease of $A_2\omega$ as a function of Δz in Figure 6b using Equation 1.

One should also note that an electrostatic interaction between tip and sample can contribute to the $A_2\omega$ signal. In particular, due to their difference in potential a positive (negative) electric charge on the sample induces a negative (positive) charge on the tip; thus, tip and sample attract each other. Consequently, an oscillation at ω of the charge on the sample results in an oscillation at 2ω of the cantilever deflection. The topography and the acoustic image (acquired at Δz = 100 nm), reported in **Figure 7**a and b, respectively, clearly show that the $A_2\omega$ signal is mainly related to the current flow in the SWCNTs and not to the electrostatic interaction between charges and induced charges on sample and tip, respectively. The agglomerate, marked as "A" in the inset, is visible in the topography while it is not visible in the corresponding acoustic image; i.e., no $A_2\omega$ signal is recorded due to material not in contact with the electrodes. Moreover, the $A_2\omega$ signal from the SWCNTs, marked with "B", (which contacts only one electrode) is not observed over the whole SWCNT, but is measured only on the portion nearest to the electrode. If electrostatic interaction had been responsible for the detected $A_2\omega$ signal, the latter would have been observed across the entire SWCNT. This suggests the presence of a spurious electric current pathway that excites thermoacoustic emission from the initial portion of the SWCNTs. An additional feature of $A_2\omega$ images is that grains and agglomerates, either on SWCNTs or on the electrodes, appear darker than the SWCNTs or electrode beneath. We attribute this result to the effect of electrostatic interaction, which is antagonist to the main thermoacoustic effect. The latter causes the displacement of the cantilever due to the acoustic wave propagating in air and, thus,

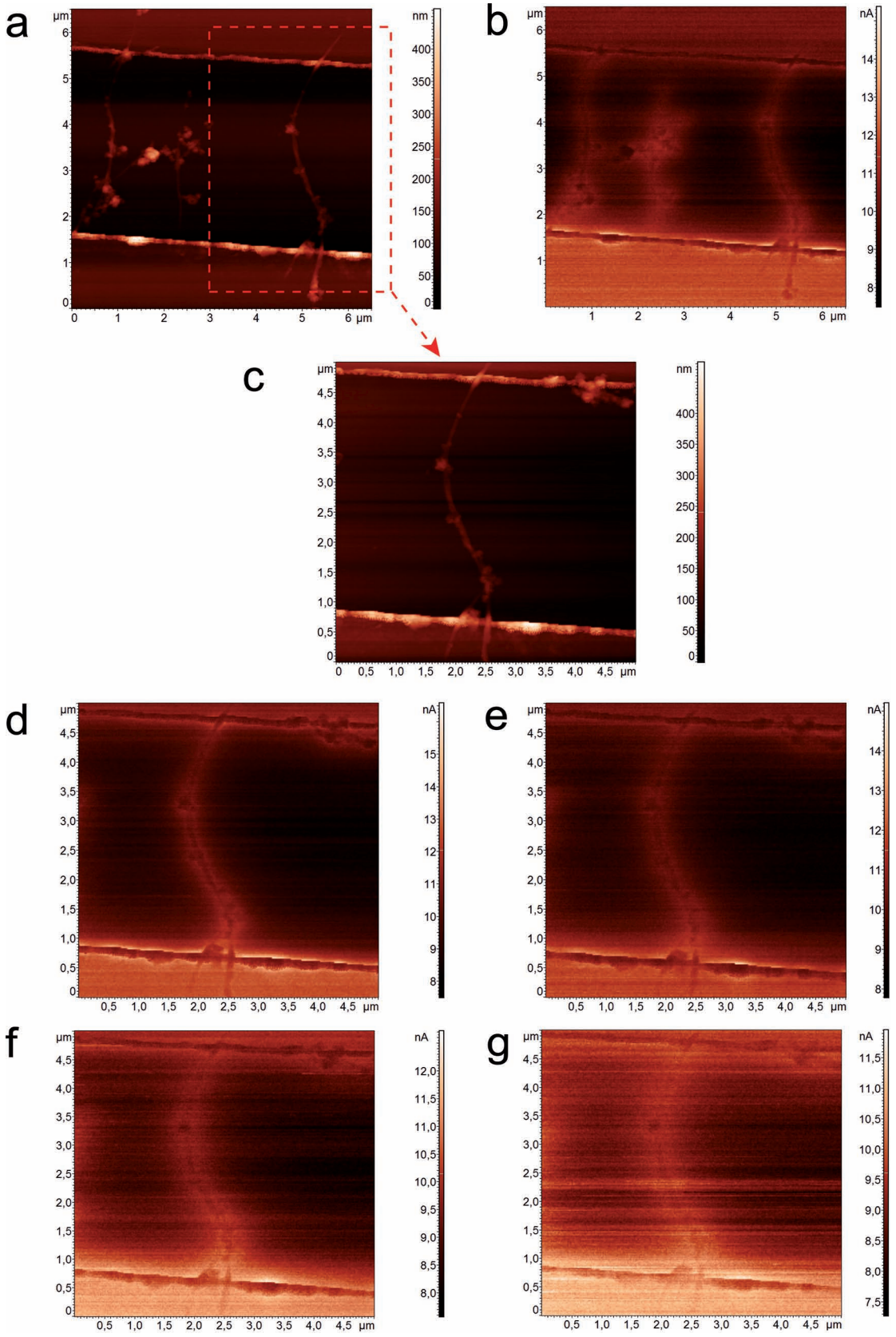

Figure 5. Topography (a) and acoustic image (b) of three SWCNT bundles contacting the two electrodes. c) Detail of one bundle with the corresponding acoustic image obtained for: $\Delta z = 50$ nm (d), 150 nm (e), 250 nm (f), and 350 nm (g).

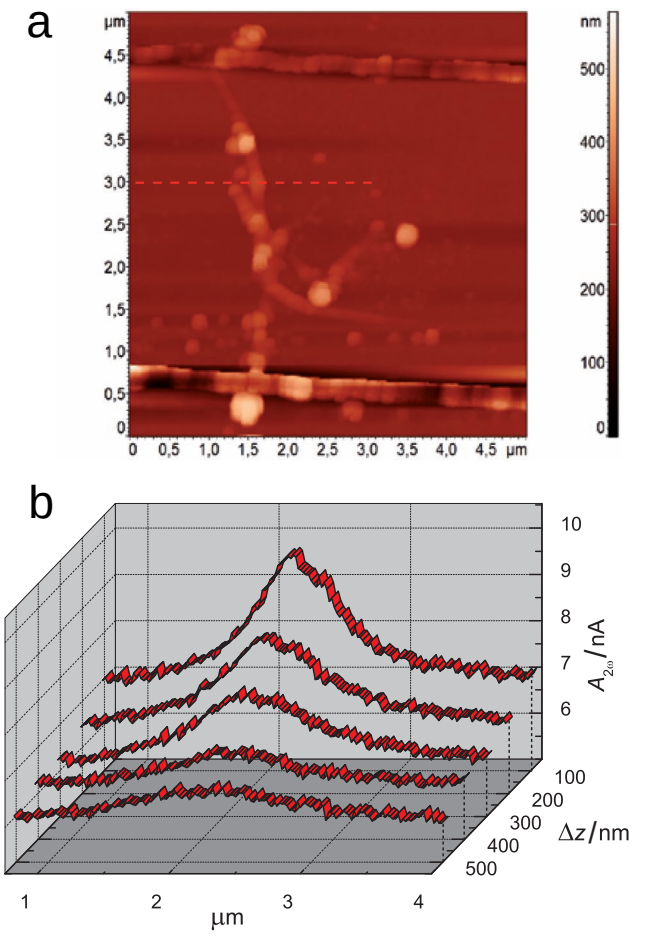

Figure 6. a) Topography of an SWCNT bundle. b) $A_2\omega$ curves acquired for different values of Δz, corresponding to the dashed line in (a).

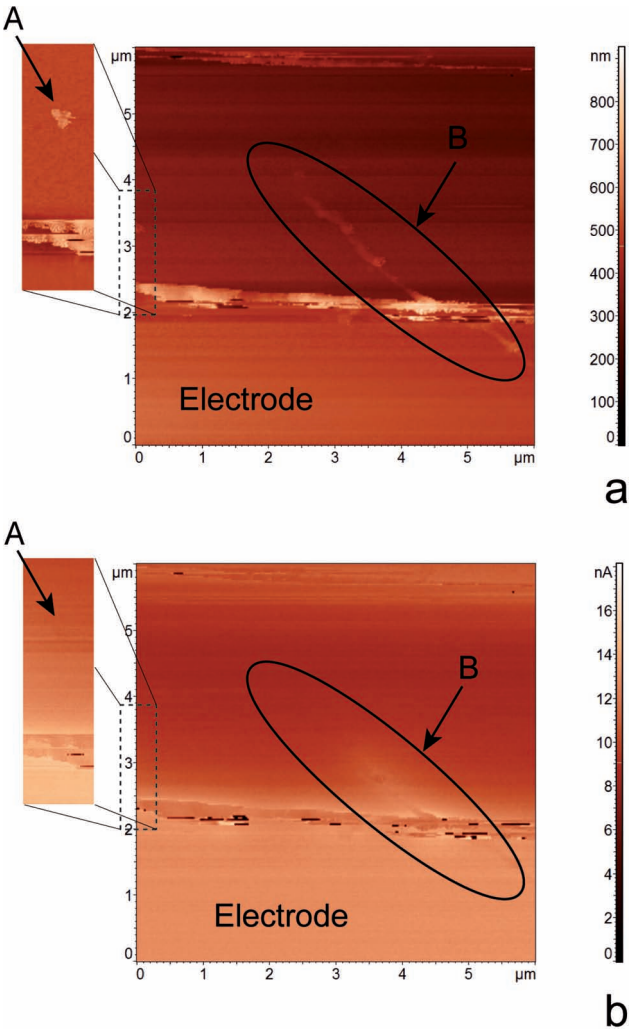

Figure 7. Topography (a) and corresponding acoustic image (b) of a portion of the SWCNT multifinger showing that material not in contact with the electrodes (marked with A, in the inset) does not produces $A_2\omega$ signal and that SWCNTs contacting only one electrode (marked with B) do not produce an $A_2\omega$ signal over their whole length.

corresponds to a repulsive interaction between tip and sample. Conversely, the effect of electrostatic interaction is attractive and is enhanced by the agglomerates that act as tips. Therefore, we should observe a reduction of the thermoacoustic signal corresponding with the grains. To verify our hypothesis, we obtained $A_2\omega$ images when applying an alternating voltage between the tip and the short-circuited electrodes. Under such experimental conditions, the thermoacoustic emission is suppressed while the electrostatic interaction is enhanced. The $A_2\omega$ signal has, indeed, a merely electrostatic origin and thus it is enhanced in correspondence with the same agglomerates that consequently appear brighter than the beneath sample (images not shown for sake of brevity). Despite the presence of a residual electrostatic interaction effect, this second experiment confirms that the origin of the contrast in the images obtained using the setup depicted in Figure 3 is primarily due to the oscillation induced by thermoacoustic emission from the sample. Therefore, it indicates that our technique is a powerful tool for the study of nanostructured thermoacoustical emitters.

4. Conclusions

We report the first experimental observation of thermoacoustic emission from isolated SWCNTs, carried out using an AFM-based technique specifically developed for this task. The capability of our technique to probe the acoustic wavefront with nanometrical lateral resolution will allow future works to verify the performances of other nanostructures. This will enable selection of the most suitable of them as building blocks for the development of new thermoacoustic emitting devices.

Received: February 11, 2012
Revised: March 21, 2012
Published online: April 17, 2012

[1] W. H. Preece, *Proc. R. Soc. London* **1879**, *30*, 408.
[2] P. de Lange, *Proc. R. Soc. London, Ser. A* **1915**, *91*, 239.
[3] H. D. Arnold, I. B. Crandall, *Phys. Rev.* **1917**, *10*, 22.
[4] E. C. Wente, *Phys. Rev.* **1922**, *19*, 333.
[5] H. Shinoda, T. Nakajima, K. Ueno, N. Koshida, *Nature* **1999**, *400*, 853.
[6] T. Kihara, T. Harada, M. Kato, K. Nakano, O. Murakami, T. Kikusui, N. Koshida, *Appl. Phys. Lett.* **2006**, *88*, 043902.
[7] A. O. Niskanen, J. Hassel, M. Tikander, P. Maijala, L. Grönberg, P. Helistö, *Appl. Phys. Lett.* **2009**, *95*, 163102.
[8] R. Venkatasubramanian, *Nature* **2010**, *463*, 619.
[9] L. Xiao, Z. Chen, C. Feng, L. Liu, Z. Q. Bai, Y. Wang, L. Qian, Y. Zhang, Q. Li, K. Jiang, S. Fan, *Nano Lett.* **2008**, *8*, 4539.
[10] M. E. Kozlov, C. S. Haines, J. Oh, M. D. Lima, S. Fang, *J. Appl. Phys.* **2009**, *106*, 124311.
[11] K. Suzuki, S. Sakakibara, M. Okada, Y. Neo, H. Mimura, Y. Inoue, T. Murata, *Jpn. J. Appl. Phys.* **2011**, *50*, 01BJ10.
[12] A. E. Aliev, M. D. Lima, S. Fang, R. H. Baughman, *Nano Lett.* **2010**, *10*, 2374.
[13] A. S. Barnard, M. L. Terranova, M. Rossi, *Chem. Mater.* **2005**, *17*, 527.
[14] M. L. Terranova, S. Orlanducci, A. Fiori, E. Tamburri, V. Sessa, M. Rossi, A. S. Barnard, *Chem. Mater.* **2005**, *17*, 3214.
[15] S. Orlanducci, E. Tamburri, M. L. Terranova, M. Rossi, *Chem. Vap. Deposition* **2008**, *14*, 241.
[16] L. Shi, S. Plyasunov, A. Bachtold, P. L. McEuen, A. Majumdar, *Appl. Phys. Lett.* **2009**, *77*, 4295.
[17] J. P. Small, L. Shi, P. Kim, *Solid State Commun.* **2003**, *127*, 181.
[18] A. Majumdar, *Annu. Rev. Mater. Sci.* **1999**, *29*, 505.
[19] B. Cretin, *Superlattices Microstruct.* **2004**, *35*, 253.
[20] M. L. Terranova, M. Lucci, S. Orlanducci, E. Tamburri, V. Sessa, A. Reale, A. Di Carlo, *J. Phys. Condens. Matter* **2007**, *19*, 225004.